Toward a brightness upgrade to the SwissFEL: A high gradient traveling-wave rf photogun

Thomas Geoffrey Lucas,[*] Hans-Heinrich Braun, Paolo Craievich, Reto Fortunati, Natalia Kirchgeorg, Anastasiya Magazinik, Marco Pedrozzi, Jean-Yves Raguin, Sven Reiche, Mattia Schaer, Mike Seidel,[†] and Riccardo Zennaro
Paul Scherrer Institut, Forschungsstrasse 111 5232 Villigen PSI, Switzerland

David Alesini and Anna Giribono
INFN–Laboratori Nazionali di Frascati, Via E. Fermi 54, Frascati (Roma) 00044, Italy

(Received 31 March 2023; accepted 19 September 2023; published 19 October 2023)

The first generation of S-band injectors for free-electron lasers has illustrated high reliability and performance by driving the latest generation of high brightness machines. However, the ultimate electron beam brightness of these devices is limited by the electric field that they can achieve on the cathode. With the aim of a higher beam brightness at SwissFEL, this paper presents the design of a C-band traveling-wave (TW) radio-frequency photogun that aims to offer the possibility to move to a cathode gradient up to 200 MV/m. This increased gradient comes from the ability to operate with rf pulse lengths approximately an order of magnitude shorter than the current state-of-the-art room-temperature S-band standing-wave rf photoguns. With this high cathode gradient, this novel gun is able to produce an electron bunch whose 5D beam brightness is 5 times greater than the current SwissFEL photogun. Furthermore, the low power dissipation within the photogun, resulting from the short rf pulse length and TW philosophy, opens up the opportunity for rf pulse repetition rates up to 1 kHz.

DOI: 10.1103/PhysRevAccelBeams.26.103401

I. INTRODUCTION

The Swiss free-electron laser (SwissFEL) is a compact x-ray free-electron laser (FEL) that has been in regular user operation since early 2019 [1]. Future upgrades to SwissFEL will aim to significantly increase the electron bunch brightness in order to produce even more brilliant x-ray beams. The ultimate brightness achieved in an FEL is limited by the electron bunch properties at the beginning of the machine, where the bunch brightness at the cathode represents the highest possible brightness that can be achieved downstream at the undulator [2]. One means of increasing this brightness at the cathode is by moving to greater electric fields on the cathode. These higher electric fields hastily accelerate the electrons to the relativistic regime, which assists in the mitigation of the detrimental effects of space charge [2]. As a consequence, one can use higher charge densities at the cathode. How to achieve these higher cathode electric fields, without degrading the operational reliability through an increased rf breakdown rate, is an issue that must be addressed. In this paper, we present the design of a traveling-wave (TW) radio-frequency (rf) photogun and propose its use to upgrade the current injector of SwissFEL. This paper aims to complement and continue on from the work previously published in [3]. This past paper primarily investigated the beam dynamics of a TW rf photogun without going into detail on the realization and operation of the gun. In this paper, we present a detailed description of a new TW rf photogun design, which will be realized as part of the IFAST project.

Section II will begin by presenting the case for a high-gradient TW rf photogun with its benefits and drawbacks. Section III will start by reviewing the previous TW rf photogun's design. A tolerance study will demonstrate the need to develop a new rf design, providing the motivation for this work. A comprehensive description of the new TW rf photogun's rf design will be given, along with the mechanical design. Using the electromagnetic simulations of the rf design, Sec. IV will illustrate how the low average power dissipation within the TW rf photogun paves the way for operation with rf pulse repetition rates up to 1 kHz. In Sec. V, the vacuum performance, which is key to the high power performance of the rf photogun and to maintaining cathode integrity, will be analyzed using state-of-the-art molecular flow simulations.

[*]Corresponding author: thomas.lucas@psi.ch
[†]Also at EPFL-LPAP, Lausanne, Switzerland.

A key addition to all rf photoguns is a high field solenoid for emittance preservation and to prevent beam losses. Section VI will present magnetostatic simulations of the design of the solenoid proposed to accompany this photogun. Taking the electromagnetic fields from the TW rf photogun and the magnetic field of the solenoid, Sec. VII will illustrate the beam dynamics performance of the TW rf photogun when compared to the current SwissFEL baseline injector system. These will aim to demonstrate the motivation for replacing the current SwissFEL gun with this novel device.

Given the large electric fields and short rf pulse lengths, some further questions must also be addressed. Section VIII will aim to address the issue of dark current which is a inherent consequence of moving to greater surface electric fields. PIC simulations will illustrate the dark current transmission, spectrum and also make predictions of the amount of dark current produced by the TW rf photogun. Finally, Sec. IX will continue on from this to discuss other open questions which still need to be addressed and the possibilities of interesting operational concepts unique to TW guns.

II. THE CASE FOR HIGH GRADIENT TW GUNS

Future FELs will aim to generate more brilliant x-ray beams for the user community. Generating high brilliance x-ray beams relies on having a high brightness electron source at the lasing undulators. The quality of this beam is primarily dictated by the quality of the beam produced by the injector [2]. Such injectors are currently optimized around the concept of optimizing 5D brightness while keeping sliced energy spread below the level where Landau damping affects the lasing process and keeping a small transverse emittance. This section will provide the motivation for moving to higher gradient photoguns and describe why TW guns are a promising technology for future FELs. The power generated along an undulator at the longitudinal position, s, can be written

$$P_\gamma(s) = P_0 \exp\left(\frac{4\sqrt{3}\pi\rho s}{\lambda_u}\right), \tag{1}$$

where P_0 is the initial power, ρ is the Pierce parameter, and λ_u is the undulator wavelength [4,5]. This Pierce parameter is an extremely useful parameter for determining the performance of an FEL as it not only dictates the output power of the undulator but it also can be used to simply describe some of the operational conditions for the lasing process to occur. The motivation for high gradients can also be illustrated through this Pierce parameter, which can be defined as

$$\rho \equiv \left[\left(\frac{I_{\text{peak}}}{I_A}\right)\left(\frac{\lambda_u A_u}{\sigma_x}\right)^2\left(\frac{1}{2\gamma}\right)^3\right]^{1/3}, \tag{2}$$

where I_{peak} is the peak current, I_A is the Alfvén current, A_u is an undulator parameter, and σ_x is the beam size [5]. With this formula, and assuming a cylindrically symmetric beam, we find the proportionality

$$\rho \propto \left(\frac{I_{\text{peak}}}{\sigma_x^2\gamma^3}\right)^{\frac{1}{3}} \propto \left(\frac{I_{\text{peak}}}{\beta_x\epsilon_{x,n}\gamma^2}\right)^{\frac{1}{3}} \propto \left(\frac{I_{\text{peak}}}{\epsilon_{x,n}^2\gamma}\right)^{\frac{1}{3}}, \tag{3}$$

where $\epsilon_{x,n}$ is the normalized emittance in x [5]. The second step in this proportionality comes by assuming a optimal optical beta function whose beam size is given by $\sigma = \sqrt{\epsilon_x\beta_x}$. The third step assumes that $\beta \propto \epsilon_{x,n}$ which comes assumption that β_x is minimized in the undulator of an FEL. A full description of the derivation of this proportionality is given in [5]. One can express the peak current and normalized emittance as the commonly used 5D brightness, which is defined as

$$B_{5D} \equiv \frac{2I_{\text{peak}}}{\epsilon_{n,x}^2}. \tag{4}$$

This allows us to arrive at the proportionality commonly used in the motivation of high brightness beams for the optimal performance of an FEL:

$$\rho \propto B_{5D}^{1/3}. \tag{5}$$

The motivation for moving to high gradients was demonstrated in [6] and therefore we will simply state the main results from this derivation. It was illustrated that the 5D brightness from an rf photogun goes with the extracted electric field strength (E_0) as

$$B_{5D} \propto E_0^n, \tag{6}$$

where n is between 1.5 and 2 [7]. This proportionality drives the decision to move to a higher cathode electric field, commonly referred to as "gradient." The work presented in [7] describes the use of a high cathode fields for a standing-wave rf photogun. However, the argument for high gradients does not specify the requirements of a standing-wave mode. Therefore, we generalize this argument to our TW case. How to achieve these higher gradients without degrading operational reliability, through an increase in the rf breakdown rate, is a heavily studied topic in accelerator physics. One significant result which has come from the studies of many TW X-band accelerating structures is that the breakdown rate (BDR) scales strongly with the peak surface electric field (E_s) and the rf pulse length (τ). An empirical formula for this dependence was developed from the results of dozens of accelerating structures tested over many years. These results gave the proportionality [8]:

$$\text{BDR} \propto E_s^{30}\tau^5. \tag{7}$$

These studies illustrated that there is a motivation to move to shorter rf pulse lengths to achieve higher electric fields. However, as observed in the equation above, the increase in the surface electric field goes as $E_s \propto \tau^{-1/6}$. Consequently, we require a significant reduction in pulse length to see a real benefit. Furthermore, whether the exponents in this formula vary for rf photoguns is still a matter of future investigations.

The minimum pulse length that can be used, to achieve the nominal energy gain for a given input power, is determined by the filling time of the rf structure. The filling time of a standing-wave cavity is given as

$$t_{f,\mathrm{SW}} = \frac{2Q_L}{\omega} = \frac{2Q_0}{\omega(1+\beta)}, \tag{8}$$

where Q_0 and Q_L are the unloaded and loaded quality factors, respectively, and β is the coupling coefficient [9,10]. We find that designing SW photoguns with shorter filling times is possible through an increase in the coupling coefficient (β) or through an increase in frequency (ω). Such techniques have been employed on SW photogun designs past and present [11]. One such example is the SwissFEL photogun which has a $\beta = 2$ and filling time of 1 μs [12]. More recently, a C-band SW rf photogun, which is also under development as part of the IFAST programme, was designed with a $\beta = 3$ resulting in a filling time of just 165 ns [13].

Another more novel approach to reduce the filling time of photoguns is to shift to TW technology. The filling time of a TW structure is given by the formula:

$$t_{f,\mathrm{TW}} = \frac{2Q_0\mu}{\omega} = \frac{L}{v_g}, \tag{9}$$

where v_g is the group velocity, L is the length of the structure, and μ is the attenuation parameter. Comparing Eqs. (8) and (9), we find that the attenuation parameter (μ) of a TW structure is the analog of the coupling coefficient (β) in a SW cavity with respect to the filling times. Such attenuation coefficients for TW structures can be easily designed such that $\mu < 1$, therefore, the designed filling time of a TW structure is able to be much shorter than a critically coupled ($\beta = 1$) SW structure. When compared to overcoupled SW structures, the TW structure has other advantages. First, TW guns can be designed with many more cells than possible in SW structures, whose total number of cells is limited by mode separation. Second, a TW gun does not require an rf circulator as the input power passes through the structure into the output RF loads rather than being reflected back towards the power source. This makes TW guns appealing for higher frequency applications where the design of rf circulators is complicated. Furthermore, TW structures are less sensitive to design tolerances making them easier to fabricate and operate, particularly at high rf pulse repetition rates. Additionally, TW gun can use phase manipulation schemes for electron bunch compression and energy spread reduction. Finally, TW guns have the ability to operate with rf pulse lengths shorter than the filling time of the TW rf photogun while maintaining a nominal peak cathode field. The implications of this final point are expected to be wide reaching as this allows for operation with very short rf pulses and the possibility of energy modulation without beam quality degradation due to a reduced cathode field strength. This final point will be elaborated on briefly in the further discussion section.

There are some drawbacks of TW guns. TW systems generally have a wider bandwidth than SW systems. This results in them being more sensitive to changes in the rf driver stability. One must take this into account when discussing the pulse-to-pulse variation of the beam properties. Related to this is the broadband nature of TW devices which means that the modes are quite close to one another making it possible to drive multiple modes with very short rf pulses.

III. RF DESIGN OF A TW RF PHOTOGUN

Given the arguments above, a design for a TW rf photogun operating at C-band frequencies was first pursued in 2013 and published in [3] and [14]. This past paper demonstrated the beam dynamics performance of the TW rf photogun and discussed how the cell lengths were optimized. Below, we will briefly review this original rf design and discuss how it was improved upon in this new design with the ultimate goal of realization.

A. Discussion of the previous TW rf photogun design

The original aim of the project was to fabricate the original TW rf photogun design with minimal modifications [14]. This design, illustrated in Fig. 1, featured ten regular cells with a phase advance per cell of $2\pi/3$. The input coupler was a coaxial style where a waveguide coupler fed the rf into the coaxial waveguide that was guided toward the input coupling cell. A virtual cell was used to prevent the need for a very small gap between the regular coupling iris and the cathode edge. To prevent the rf from feeding upstream from the input coupler, an input filtering cell was employed. This prevented field leakage at the joint where the inner conductor was mechanically connected to the input coupler. The ability to remove this inner conductor was to allow a cathode exchange in the event of its degradation. Downstream of the regular cells, the rf is coupled out through a coaxial coupler. Similar to the input coupler, this output coaxial coupler also featured a filtering cell to prevent field leakage downstream of the output waveguide coupler. Unlike the input coupler, the output coupler had an rf choke placed along the coaxial waveguide. The function of this rf choke was to allow the

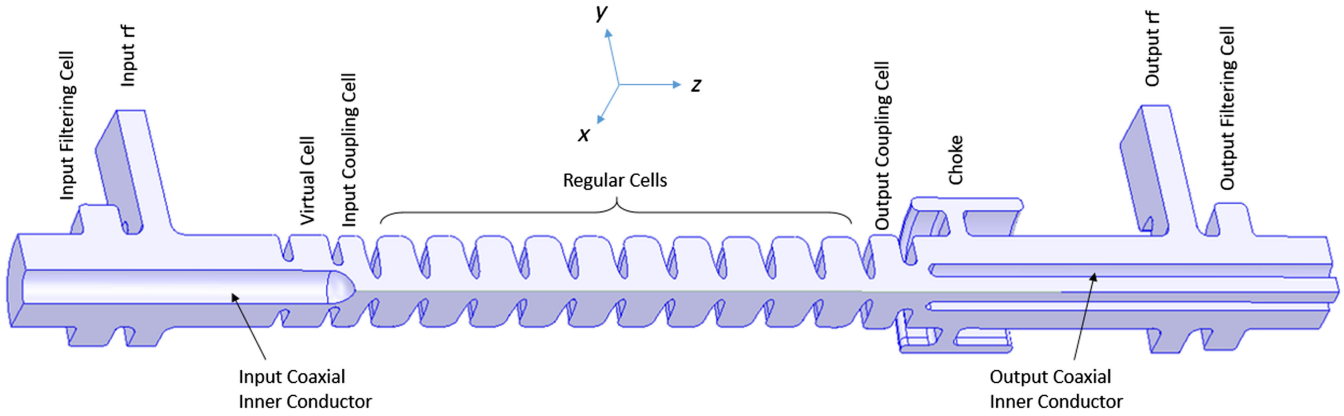

FIG. 1. Original design for the TW rf photogun with the major components labeled [3,14].

output coupler to be removed in order to place the solenoid around the rf photogun. Given that this design featured mechanically removable components of the coaxial input and output couplers, it was important to understand the tolerance requirements when reattaching these in order to determine the complexity of operating this device. A tolerance study on the allowable error in the alignment of these inner conductors when mounted was performed for the input and output rf couplers. This study was performed using CST's frequency-domain solver, using 9.15 million tetrahedral cells, and the results are illustrated in Fig. 2 [15].

A major finding of the tolerance study was that the long inner conductor of the input coupler was very sensitive to translational and angular misalignments in the y and z axes where the y axis represents the plane where the input couplers are located and the z axis is the beam axis. Taking the example of a 200-μm translation in the y plane, a reasonable misalignment possible when mechanically mounting a flange, one observes an increase in the reflected power from the input coupler from −35 dB to −12 dB. Similar results were also found when the cathode was tilted in this plane. This inner conductor was designed to be

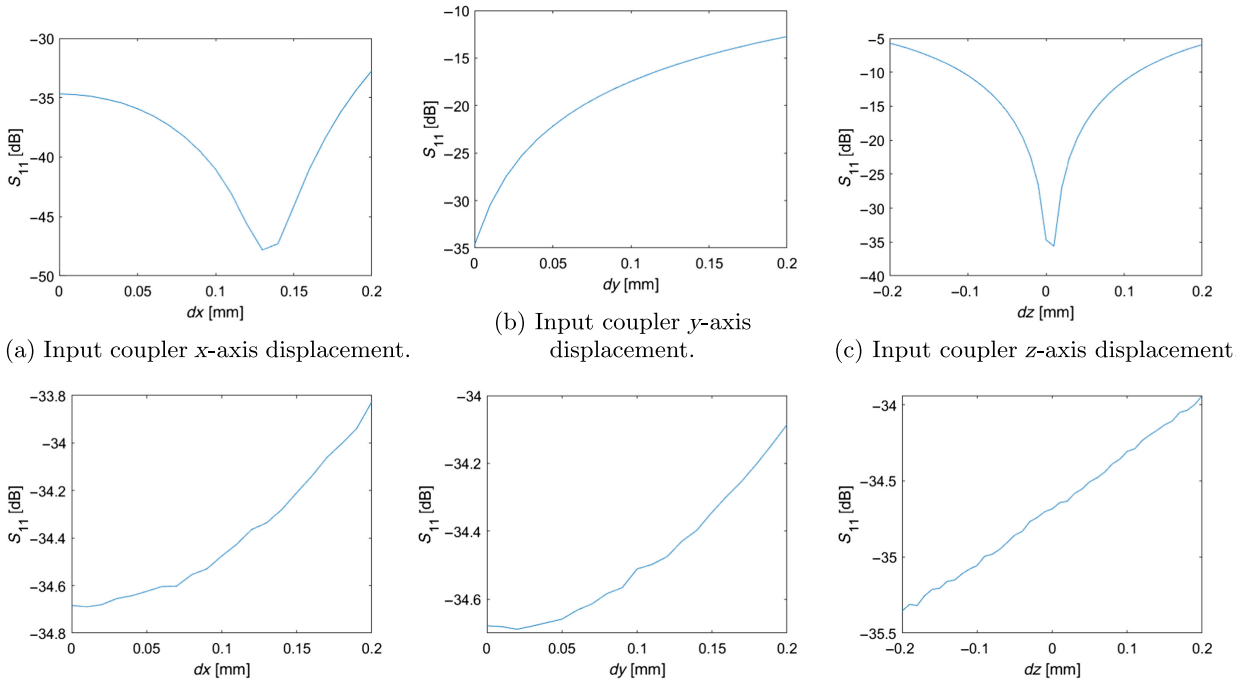

(a) Input coupler x-axis displacement.

(b) Input coupler y-axis displacement.

(c) Input coupler z-axis displacement.

(d) Output Coupler x-axis displacement.

(e) Output Coupler y-axis displacement.

(f) Output Coupler z-axis displacement.

FIG. 2. The tolerance study results for the original TW rf photogun design from the input coupler's (top) and output coupler's (bottom) inner conductor. The terms dx, dy, and dz represent an offset of the inner conductor in the two transverse axes and the longitudinal axis, respectively.

exchangeable to allow the cathode to be replaced during operation. Given this, it was concluded that realigning this inner conductor, every time the cathode was exchanged, would be very complicated during normal SwissFEL operation and, therefore, a more robust solution was required. In order to fix this alignment sensitivity, it is important to understand its root cause. Further investigation into the alignment sensitivity found two causes. The first cause was an asymmetry in the phase advance within the coaxial waveguide which resulted from the offset of the inner conductor toward the rf input couplers. The second cause was a perturbation of the volume of the input coupling cell when the cathode was shifted, which led to a change in its resonant frequency. With this insight, it was determined that it would be possible to correct these changes in the reflected power caused by such coaxial misalignments through the use of a phase shifter on one input waveguide port, amending cause 1 and an offset of the inner conductor in the z axis, amending cause 2. Figure 3 demonstrates the reflected power (S_{11}) for various phase differences between the two input ports and for various translations of the inner conductor in z-axis for the situation of a 200-μm misalignment in the cathode in the y axis. The cross within the figure illustrates the reflected power without a phase difference between the input ports or an adjustment to the inner conductor in the z axis. It is observed that with a 50-μm shift in the z axis and a phase difference of 0.15 radians between the input ports, one could re-establish the nominal reflected power of < -45 dB, illustrated as a circle. However, this technique does not fix the possible changes to the beam dynamics resulting from the asymmetric field profiles on the cathode caused by such a translation.

The tolerance study was repeated for the output coupler's inner conductor. Interestingly, this inner conductor misalignment issue was not observed on the output coupler. The reasons for this were the following. The volume of the output coupling cell did not contain the inner conductor therefore shifts in its location would not perturb the volume of this cell. Additionally, any asymmetry in the phase advance of the coaxial waveguide on the output coupler would be seen at the two rf outputs of the gun. These are simulated as separate outputs in the electromagnetic simulations and therefore do not affect one another. In practice, this means that it is important that such rf waveguide outputs are terminated separately with individual rf loads or if they are combined, the phases should be carefully matched to compensate for any phase advance. In summary, the tolerance study determined only the input coupler required a new conceptual design for the style of coupler.

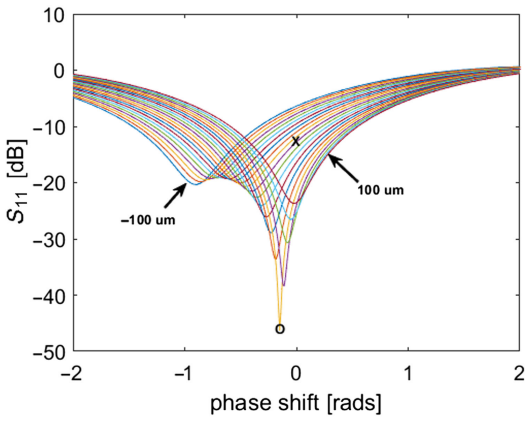

FIG. 3. Amending the reflection (S_{11}) through an added phase shift on one input power and through tuning in z. Different colors represent shift of the cathode in z between −100 μm and 100 μm. The cross represents the reflection given a 200 μm error in the y axis and the circle represents the reflection after the two step amendment.

Despite only the input coupler suffering from the severe tolerance issues, there were further features that were considered undesirable in the rf design. The use of rf chokes and filtering cells in the original design resulted in a complex rf design that was possibly prone to multipacting [16]. The choke was added to the original design to allow the output coupler to be removable in order to assist in the mounting of the main solenoid. The filtering cells, added to both the input and output couplers, aimed to reduce the fields at the location where the inner conductors of the two coaxial waveguides were mechanically connected to the flange. With all of the results above in mind, it was decided that an updated TW rf photogun design should be modified such that: (1) It was less sensitive to fabrication tolerances whether that be through a new design or more robust joining of the inner conductors; (2) it should remove all rf chokes and filtering cells while still being able to mount the solenoid around the structure; (3) the rf lengths of the regular cells, input coupling cell, and output coupling cell were extensively optimized in the original design and therefore it was desirable to leave these dimensions unchanged. With these points in mind, a design study of the new rf input and output couplers was undertaken.

B. Updated input coupler

Given the tight alignment tolerances of the inner conductor in the input coupler, it was important that the inner conductor could be fixed in place with brazing rather than mechanically aligned each time the cathode was removed. For this reason, the original electrically coupled input coupler was exchanged with a magnetically coupled input coupler with coupling slots. These coupling slots are visible in both the vacuum and mechanical models, illustrated in Figs. 4 and 5, respectively. The use of coupling slots rather than the freely hanging inner conductor that formed a coupling iris, used in the original design, allowed the inner conductor of the coaxial waveguide to be joint to the outer conductor. Consequently, it needed to be aligned only once during the assembly after which it is brazed in place. This could be done to significantly higher precision than a inner

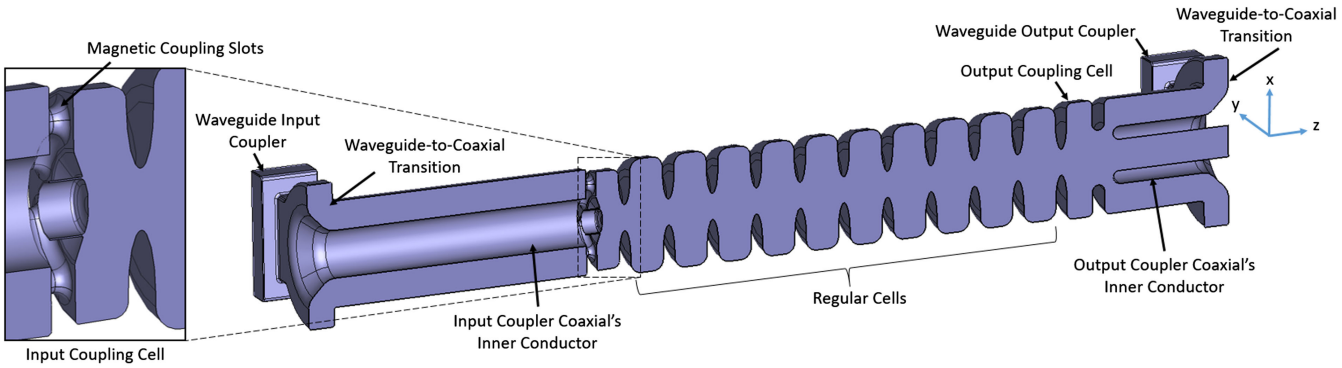

FIG. 4. Vacuum design of the TW rf photogun with annotations of the key components.

conductor mechanically attached using a beampipe flange. As a consequence of this new design, the input filtering cell and virtual cell of the original design could be removed from the design reducing the overall complexity.

To keep the possibility of a replaceable cathode, the inner conductor for the input coaxial was designed to be hollow with the cathode inserted through the center of the inner conductor. This new concept is illustrated in the mechanical diagram (Fig. 5). The cathode plug, visualized in cyan, is placed at the end of a rod and inserted through the center of the inner conductor of the input coaxial waveguide. This new design also allowed for a cathode plug design similar to that of the current SwissFEL rf photogun [17]. This was important when considering the possibility of the TW rf photogun's use in SwissFEL, which would require a load-lock capability. The gap between the rod, which holds the cathode plug, and the inner conductor was enlarged to improve vacuum pumping behind the cathode. Additionally, the cathode plug had wedge-shaped slots cut into it to provide better pumping in the region of the rf contact spring. The total length of the input coaxial waveguide was primarily driven by the dimensions of the main solenoid and bucking coil that will be described below. Finally, an additional chamfer was added to the waveguide-to-coaxial transition of the coupler.

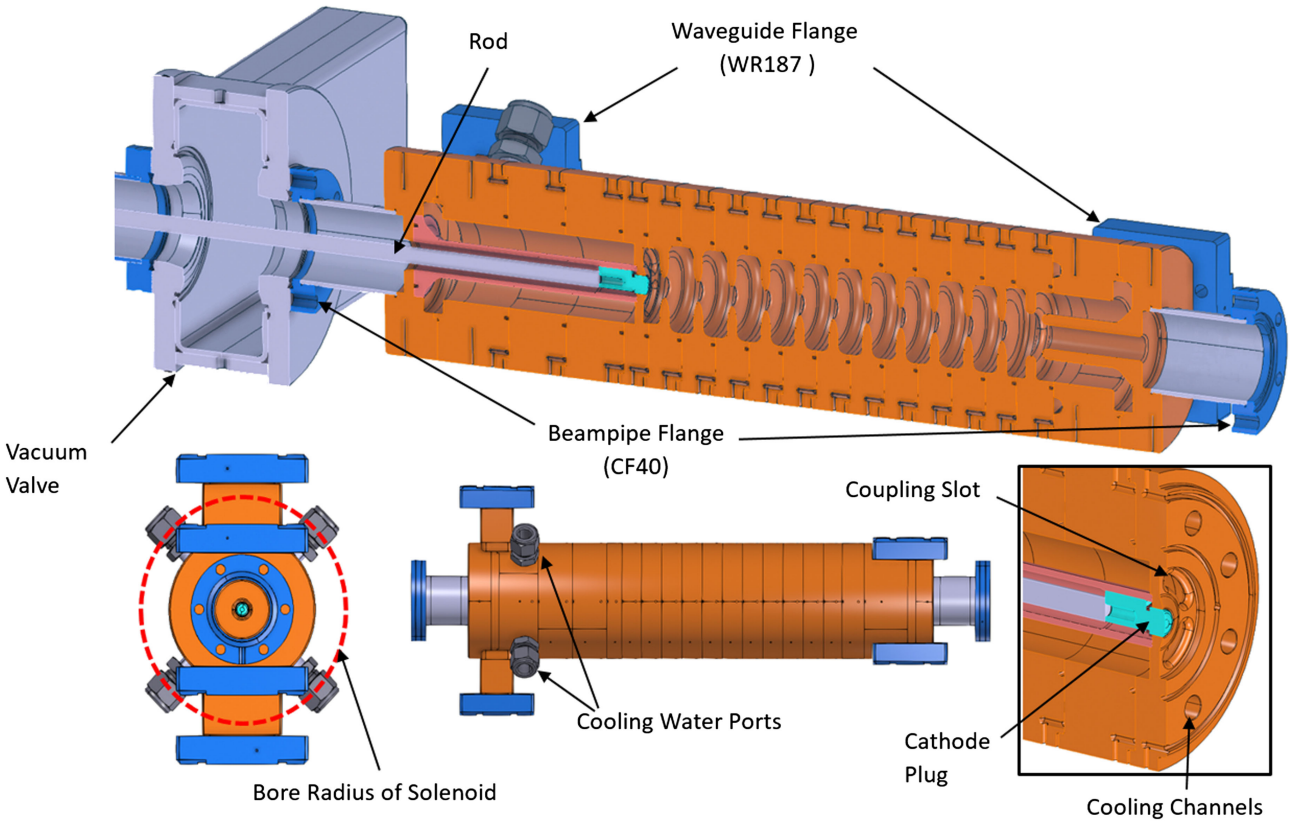

FIG. 5. Diagrams of the mechanical design of the TW rf photogun with annotations.

The functionalities driving the motivation for this chamfer are twofold. The first was an increase in the coupler's bandwidth from 53 to 100 MHz when considering the region where the reflection is less than −30 dB. The second functionality was to remove the local minimum in the electric field magnitude that occurred between the inner conductor and cell wall. This local minimum is a region that could be prone to multipacting and therefore removing it was thought to be prudent [18].

C. Updated output coupler

For the output coupler, the tolerance study illustrated that the concept of a "free-hanging" inner conductor was feasible and that it did not require coupling slots, as was the case for the input coupler. However, the presence of the rf chokes and filtering cells was still something that needed to be addressed. In order to remove the need for the rf choke and output filtering cell, while also allowing the solenoid to be placed over the TW rf photogun, the output coupler needed to be redesigned. This was because the original waveguide arms were too long to slip a solenoid, of reasonable bore radius, over the end. A new radially compact rf coupler was designed with the aim that the waveguide flanges have a maximum radius of less than 70 mm. The reduced radius allows for the main solenoid and bucking coil to be placed over the TW rf photogun without the need to dismount the entire output coupler, as was proposed in the original design. Without the rf choke and output filtering cell, the length of the output coaxial waveguide was reduced drastically from 150 to 50 mm. The minimum length of this output coaxial waveguide was ultimately limited by the mechanical design. This design sees the WR187 waveguide flange embedded into the photogun body to keep the outer radius of the output coupler below 70 mm (Fig. 5). As was implemented in the input coupler, the output coupler also had a chamfer added to remove this undesirable local electric field minimum and increase the coupler bandwidth.

D. Regular cells

In [3], extensive beam dynamics calculations were performed to optimize the length of the input coupling cell and choose the optimal phase advance. For this reason, it was decided that the regular cell geometry of the new gun would be the same as in the original design. Two separate phase advances were investigated as part of this original study. It was found that a phase advance of $\pi/6$ performed better in terms of beam dynamics performance, with the 5D brightness achieved 50% greater than that of the $2\pi/3$ case given a cathode gradient of 135 MV/m. However, the shunt impedance was considerably lower resulting in a 54%

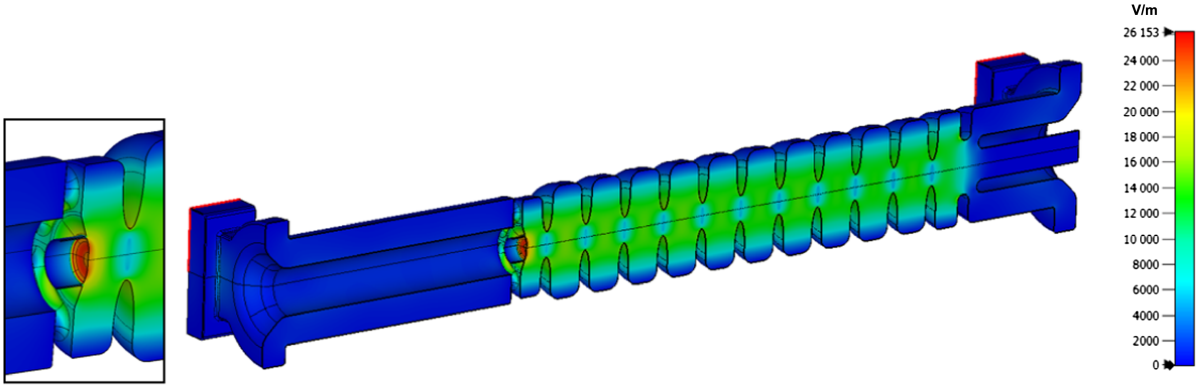

(a) Electric field.

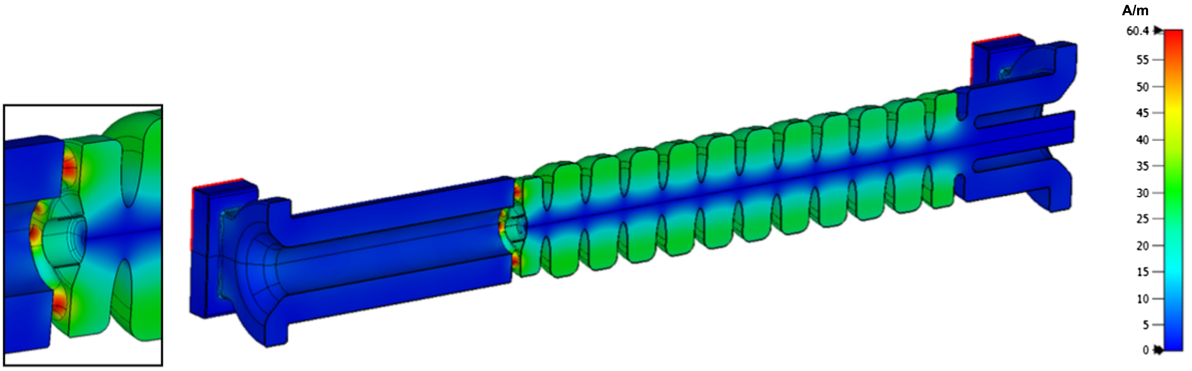

(b) Magnetic field.

FIG. 6. The absolute magnitude of the electric and magnetic fieldmaps within the TW rf photogun for a peak input power of 1 W.

increase in the power requirements. For this reason, it was decided that the new design would use the $2\pi/3$ phase advance. Given the low power dissipation and low number of total regular cells, a constant impedance design was chosen. Finally, to also keep with the philosophy of not changing features that would affect the beam dynamics simulations performed in the past, the total number of regular cells was kept to ten, with two additional coupling cells.

E. Electromagnetic simulations and high-power performance metrics

With the newly updated rf design, it was important to know whether any of these changes would affect the high-power performance. For this, one can use certain rf metrics to predict the performance and understand what may be the limitations. Figure 6 displays the absolute magnitude of the electric and magnetic fields for the new TW rf photogun design. It is observed that the greatest electric fields are located on the cathode. For an input power of 82 MW, the peak electric field at the center of the cathode is 200 MV/m. The peak electric field on the irises is 12.5% below that of the central cathode electric field and, therefore, it is expected that most breakdowns will occur on the replaceable cathode plug rather than on the cells. An important check for the new magnetically coupled input coupler was to ensure that the magnetic field on the coupling slots was not too high. For pulsed systems, a high magnetic field can cause damage through thermal stresses known as pulsed surface heating. It has been previously observed that pulsed surface heating should be restricted to below 50 K [19] to prevent cracks in the surface of the copper. The temperature rise from pulsed surface heating can be calculated through the formula

$$\Delta T = \frac{1}{2} R_s \frac{2\sqrt{\tau}|H|^2}{\rho c_\epsilon \sqrt{\pi \alpha_d}}, \tag{10}$$

where R_s is the surface resistance, τ is the rf pulse length, H is the complex surface magnetic field, α_d is the thermal

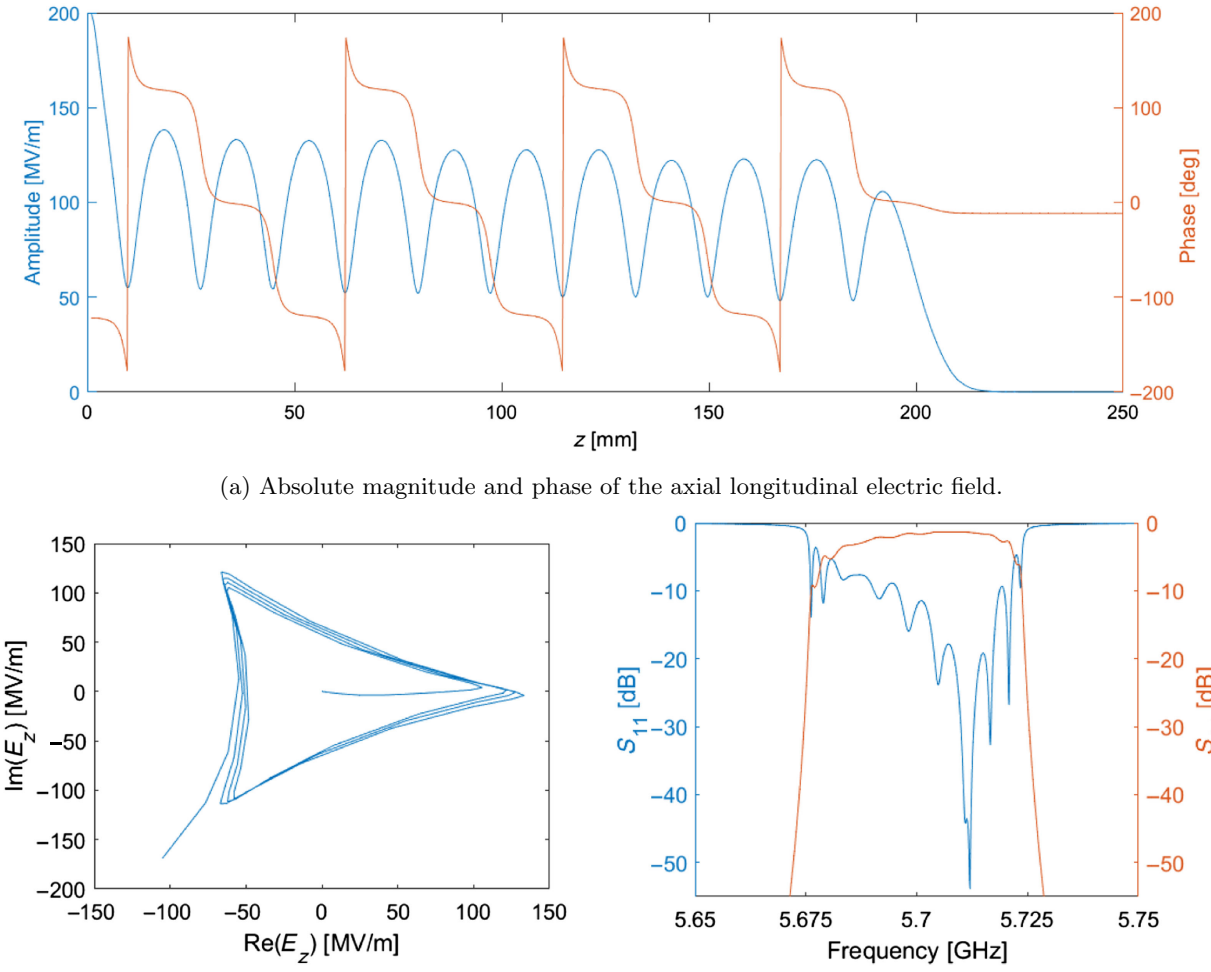

(a) Absolute magnitude and phase of the axial longitudinal electric field.

(b) Imaginary vs real axial longitudinal electric field.

(c) S-parameters from the input coupler.

FIG. 7. Electromagnetic distribution for the cells of the TW rf photogun.

TABLE I. rf parameters of the updated TW rf photogun.

Parameter	Value	Units
Frequency	5.712	GHz
No. of accelerating cells	12	
Cell length	17.495	mm
Structure active length	250	mm
Phase advance	120	°
Attenuation	−1.41	dB
Group velocity	0.79	%c
Filling time	90	ns
Input power	82	MW
Peak E field (irises)	175	MV/m
Peak E field (cathode centre)	200	MV/m
Peak H field	558	kA/m
Pulsed surface heating (100 ns)	30.6	K

diffusivity, c_ϵ is the specific heat at constant strain, and ρ is the density [19]. Taking an rf pulse length of 100 ns and a peak magnetic fields of 558 kA/m, it is found that the temperature change due to pulsed surface heating is 30 K which is below the 50-K threshold. It is observed that the electric and magnetic fields on the output coupler are much lower than the input coupler and, consequently, are not expected to cause any issues. Figures 7(a) and 7(b) depict the longitudinal electric field along the beam axis. These plots illustrate a well-tuned structure with a peak central cathode field of 200 MV/m. Finally, the S parameters [Fig. 7(c)] are found to give a reflection less than −40 dB, an attenuation of −1.41 dB and a total bandwidth of 3 MHz for a reflection below −30 dB. A comprehensive list of rf parameters is included in Table I. To ensure the accuracy of the rf simulations, all ANSYS HFSS simulations were also verified with simulations in CST's frequency-domain solver, which found similar results [20].

F. Tolerance requirements

Using the same methodology as the tolerance study performed for the previous design, the couplers were investigated for their sensitivity to misalignments. The simulations were performed in CST's frequency domain solver with approximately 15.5 million tetrahedral mesh cells. The increase in mesh cells, compared to the tolerance study above, came as a result of the more complex geometry of the magnetic coupling slots. The tolerance study investigated the alignment of the inner conductor in the input and output couplers. The advantage of the new design is that the inner conductors of the two coaxial couplers are automatically aligned by the mechanical geometry and then brazed in place. Consequently, the alignment only has to occur once. Nevertheless, it is important to understand the requirements for the initial assembly. Figure 8 illustrates the results of the tolerance study. These results illustrate that the new input coupler is

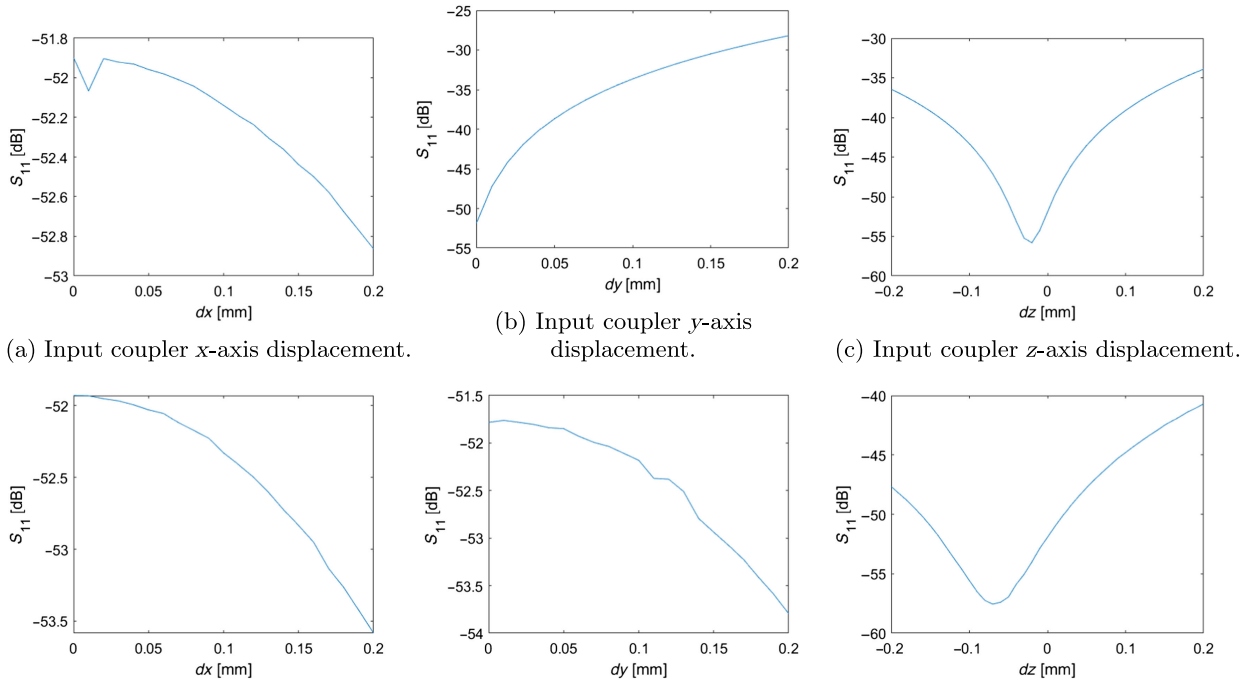

(a) Input coupler x-axis displacement.
(b) Input coupler y-axis displacement.
(c) Input coupler z-axis displacement.
(d) Output coupler x-axis displacement.
(e) Output coupler y-axis displacement.
(f) Output coupler z-axis displacement.

FIG. 8. The tolerance study results for the updated TW rf photogun design from the input coupler's (top) and output coupler's (bottom) inner conductor. The terms dx, dy, and dz represent an offset of the inner conductor in the two transverse axes and the longitudinal axis, respectively.

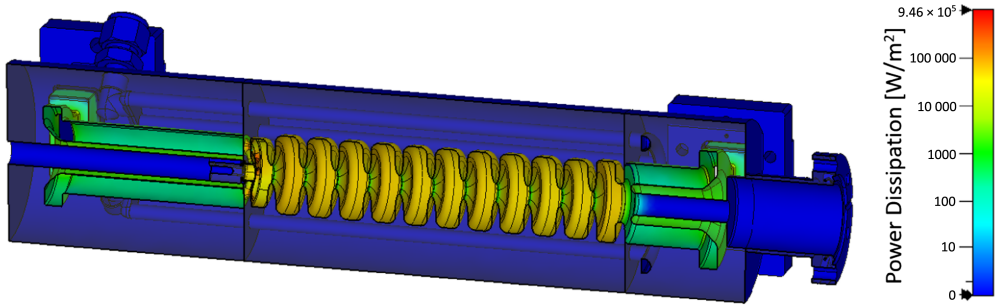

(a) Power dissipation.

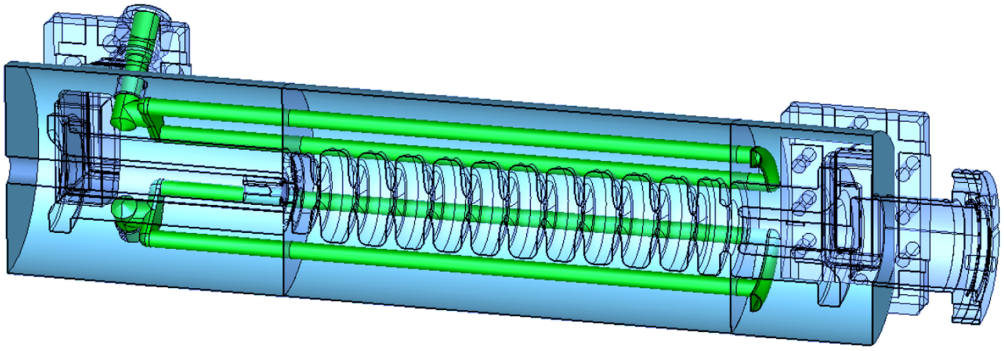

(b) Cooling Channels.

FIG. 9. Sources of input and output power for the thermal simulations. Input power comes from rf power dissipation and the total power dissipation is illustrated for the 1 kHz operation case. The cooling comes from the cooling water flowing (green) and the heat dissipation to the surrounding environment (blue).

still sensitive to the offset of the coaxial toward the wall. However, due to the better matching of the new design, we find that an offset of up to 200 μm is still tolerable. The coaxial is extremely insensitive to offsets in the axis perpendicular to the couplers where we see that even for an offset of 200 μm, the coupling remains below −50 dB. A misalignment in the longitudinal dimension, z, also does not lead to a significant change in the matching. For the output coupler, we find that the tolerances are even less sensitive to changes and misalignments up to 200 μm in all axes still achieve a matching below −40 dB.

IV. THERMAL SIMULATIONS OF HIGH REPETITION RATE OPERATION

Operation at higher rf pulse repetition rates is desirable for future FELs. Given its short filling time and low attenuation, the TW rf photogun has the ability to operate at a very high rf pulse repetition rates. In order to understand what may limit this repetition rate, steady-state thermal simulations of the TW rf photogun were performed in CST's thermal and mechanical solver. The simulations performed were unidirectional and do not account for the expansion of the TW rf photogun with a change in temperature. However, the simulations aim to illustrate the temperature change in the regions known to be more temperature sensitive, i.e., have a narrow bandwidth. In the case of the TW rf photogun, these are the regular cells and input coupling cell.

The simulations began by coupling the electromagnetic solver results, in particular, the surface power dissipation, to the thermomechanical solver. This surface power dissipation is illustrated in Fig. 9(a). The transfer of heat out of the system was assumed to occur through two processes, the convection of heat into the cooling water and the convention of heat to the air in the surrounding environment [Fig. 9(b)]. These processes were assigned heat transfer coefficient values of 7000 $W/m^2/K$ and 5 $W/m^2/K$, respectively. These values were obtained through analytical calculations and modeling in ANSYS Fluent for a water speed of 1.5 m/s [21,22]. The cooling water was assigned a temperature such that the mean temperature of the TW rf photogun's regular cells was the nominal operational temperature of 313.15 K. The air of the surrounding environment was assigned an ambient temperature of 293.15 K. Given all temperatures were near room temperature, losses due to radiation were not included in the simulation. Conduction losses to waveguides and the mechanical support systems were assumed to be low. Figure 10 illustrates the temperature distribution for 100-Hz and 1-kHz rf pulse repetition rate operation for the nominal operational power of 82 MW and a total rf pulse length of 100 ns leading to a 10-ns stable rf time. Such values

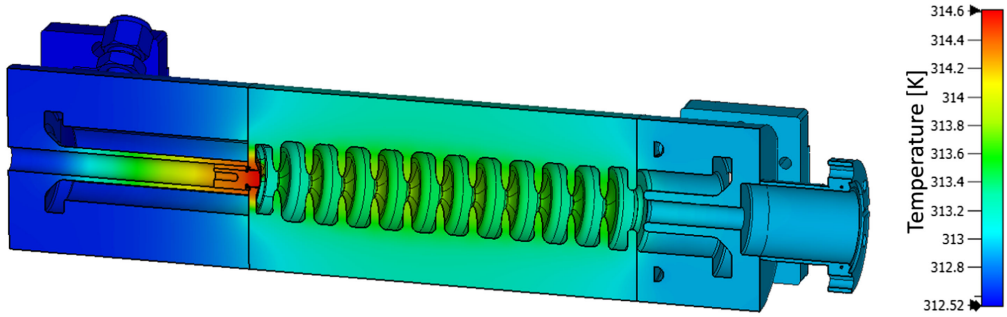

(a) 100 Hz.

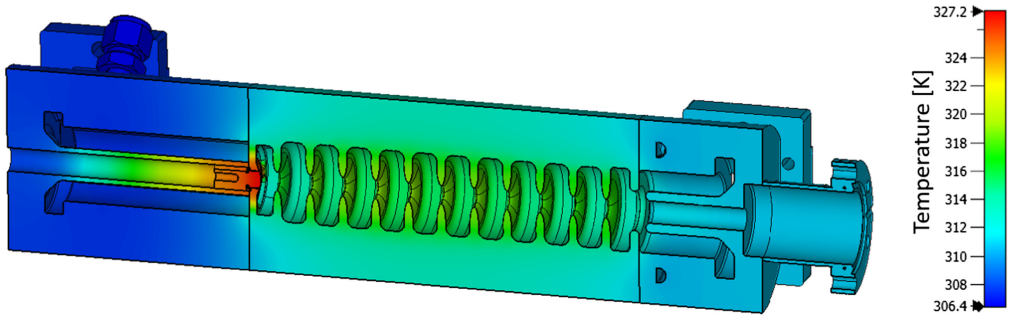

(b) 1 kHz.

FIG. 10. Thermal simulations of the TW rf photogun for two rf pulse repetition rates.

do not include the pulsed surface heating resulting from the magnetic fields of the driver rf power, mentioned above, or the pulsed heating from the photocathode laser, which will be elaborated on below in the further discussion. It is found that for 100 Hz operation, the maximum steady-state temperature within the TW rf photogun is 1.45 K above the nominal operational temperature while for 1-kHz operation, this increases to 14.05 K. This maximum temperature occurs on the region of the cathode adjacent to the magnetic coupling slots where the power dissipation is greatest and in a region that is more thermally isolated due to the presence of the magnetic slots and gap between the cathode plug and inner conductor. It will be important to establish a good contact between the removable cathode plug and the inner conductor of the input coupler to prevent overheating of the cathode. It is to be seen whether an adjustment of the cathode's position to rematch the coupling of the input coupling cell is required due to the temperature increase. However, the total length of the cathode plug is expected to increase only 6 μm for a 14-K temperature increase, which is within the required machining tolerances. Along with the increased temperature of the cathode, the temperature decreases around the waveguide-to-coaxial transition where the power dissipation is low. This is particularly noticeable in the input coupler. Given the very wide bandwidth of the waveguide-to-coaxial transition, it is expected that this temperature difference will not affect the performance of the TW rf photogun. These results illustrate that 1-kHz operation is feasible for this device with respect to power dissipation.

V. PERFORMANCE AT ULTRAHIGH VACUUM

rf photoguns require extremely high vacuum levels for nominal operation, particularly to prevent the degradation of the cathode when made from a semiconductor material such as cesium telluride (Cs_2Te). Vacuum simulations of the rf photogun were performed using the Molflow+ software package [23] to ensure that within this complex geometry, the required vacuum can be obtained both for the high gradient operation of the rf photogun and the prevention of the degradation of a semiconductor cathode. The initial calculations were performed for nitrogen particles in order to generally judge the complexity of pumping the device to reasonable pressures for operation. The copper was assigned an outgassing rate of 5×10^{-11} mbar/l/s/cm^2, which is a conservative value for baked copper when considering the effect of the dynamic desorption during the gun operation. One important factor to consider will be how quickly one can pump down the structure to the nominal operating pressure after an rf breakdown. This will be the focus of investigation during the high-power testing. The vacuum simulations for N_2 are depicted in Fig. 11 for pumping rates of 50 l/s on each waveguide port and at the tee in the manipulator. It was found that the vacuum has a maximum value of 5.9×10^{-9} mbar in the central cells of

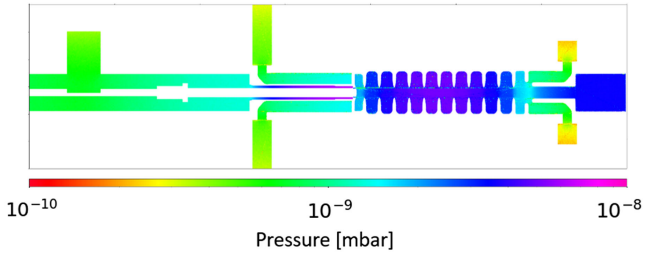

FIG. 11. The Molflow+ simulations of the rf photogun and the manipulator which will house the cathodes during the initial evacuation of the system.

the photogun. The vacuum at the cathode is approximately 1.5×10^{-9} mbar.

When pumping the gun from atmospheric pressure, the strategy will be to pump with the cathode retracted into the load-lock system. This load-lock system will already be under vacuum and separated from the TW rf photogun by a vacuum valve. The retracted cathode will ensure adequate pumping speeds inside the hollowed inner conductor region where the cathode will eventually pass through for insertion. Once the photogun has reached its minimum pressure during pumping, the vacuum valve will be opened and the cathode will then be inserted. This will ensure that any semiconductor cathode always experiences a high vacuum environment. The maximum pressure within the manipulator is located between the rod and the inner conductor where the vacuum is approximately 6.6×10^{-9} mbar. However, this value is calculated for the situation when the cathode is fully inserted. rf power is also not present inside this region so it is not expected to cause issues. The pressure within the main load-lock chamber is less than 10^{-9} mbar.

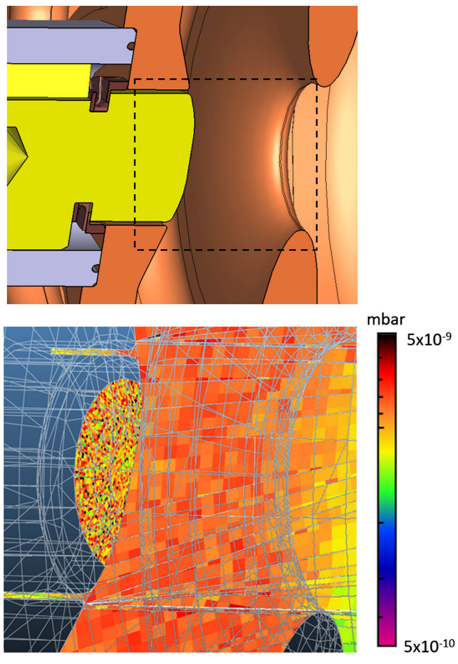

FIG. 12. The Molflow+ simulations of the rf photogun cathode cell region for water vapor. The dashed box represents the region represented in the vacuum simulation.

When considering the contributions of poor vacuum to the cathode lifetime, one must consider other gases such as water vapor, O_2, CO, and CO_2. Literature on the outgassing rate of these gases for oxygen-free high-conductivity copper are scarce. However, one source quotes the outgassing of water vapor as 3×10^{-11} mbar/l/s/cm^2 [24]. Using this outgassing rate, the simulations were performed again and the results of the pressure near the cathode, which is expected to be most affected by the water vapor, are illustrated in Fig. 12. We find that in the region of the cathode, the water vapor pressure is less than 5×10^{-9} mbar. This is a little high for semiconductors and it is to be seen whether this will cause issues for the operation of Cs_2Te cathodes.

VI. MAIN SOLENOID AND BUCKING COIL

Important for emittance preservation and beam transmission, all rf photoguns must be accompanied by a solenoid magnet. A basic design of the magnet was described in [3,14] and used for the original beam dynamics simulations. In this work, we extend upon the original simple design by creating a more realistic model that also fits the new bore radius requirement. The reader will recall that this was defined by the outer radius of the output waveguide flanges. The new model also includes power dissipation and cooling requirements. The magnetic yoke is assigned to be steel and the design aimed to keep the maximum magnetic field within the steel yoke to below 2 T. The coils an 8-by-8 mm square conductor with a 5-mm bore diameter cooling channel. Figure 13 demonstrates the solenoid model around the updated design. The design uses the same concept as the original magnet where the main solenoid and bucking coil have their yokes connected. Below the rendering is a plot of the axial magnetic field. The cathode lies at $z = 0$ where the total magnetic field is zero. This ensures no addition to the emittance due to local magnetic fields [25]. For a peak field of 0.61 T, the coils of the main solenoid require a current density of 7.01 A/mm^2. Such a value is high but still feasible for a normal conducting solenoid [26]. The temperature rise, due to the resistive losses, and cooling requirements can be estimated using the specific heat capacity equation [27]. First, the resistive power losses, due to the high current density, is 10.75 kW for the main solenoid. To cool this, keeping the temperature rise to 21 K, the cooling water must have a pressure of 2.8 bar flowing at 1.24 m/s inside the bore. Such a calculation can be performed for the bucking coil also, which has a current density of 3.22 A/mm^2. The resistive losses in the bucking coil are much lower at 906 W. Using cooling water of 0.7 bar flowing at 0.55 m/s leads to a temperature rise of just 10 K.

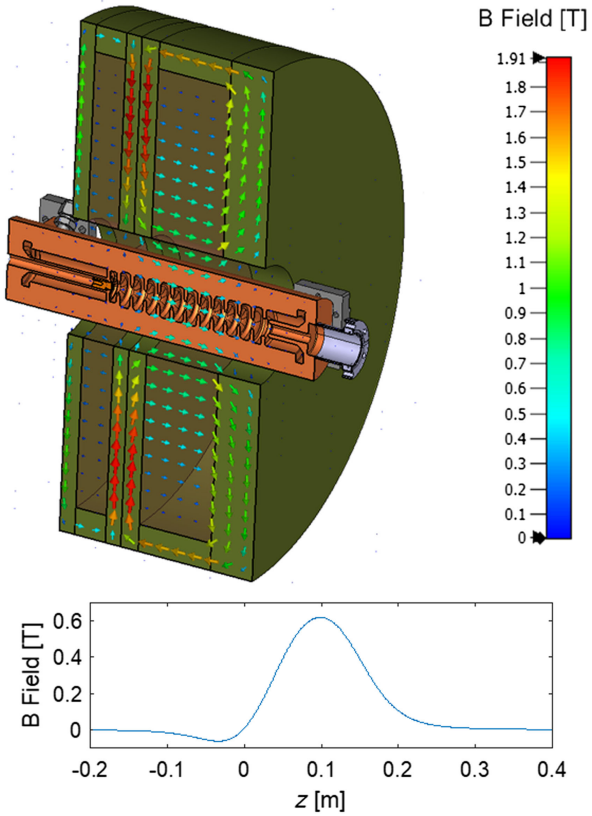

FIG. 13. Combined main solenoid and bucking coil with the axial magnetic field plotted below.

VII. BEAM DYNAMICS SIMULATIONS OF A SWISSFEL INJECTOR UPGRADE

In order to understand the possibilities of the TW rf photogun as an injector upgrade for SwissFEL, detailed beam dynamics simulations of the new photogun design were performed, along with simulations of the current SwissFEL photogun as a comparison, and to validate the new simulations against previous simulations and measurements. In [14] and [3], the beam dynamics performance at two different gradients was illustrated so here we only simulated for the high gradient case to illustrate that the beam dynamics performance is maintained. All of the beam dynamics simulations were performed in General Particle Tracer (GPT) with mesh-based 3D space charge and a Dirichlet boundary condition on the cathode [28]. For the TW rf photogun, the full 3D electric and magnetic fieldmaps were used in order to understand whether multipole components, which may result from the rf input couplers or magnetic-coupling slots, will affect the beam quality. The simulations were performed for the beginning of the SwissFEL injector, as illustrated in Fig. 14. This beamline consists of an rf photogun, with its main solenoid, along with two 4-m S-band TW accelerating structures (TWS). The two accelerating structures each are allowed to operate up to an accelerating gradient of 20 MV/m. The two TW structures each have four solenoids around them. When changing between the current SwissFEL S-band SW photogun simulation and the TW rf photogun, the only changes made to the beamline were to change the photogun and its main solenoid, and to adjust the distance between the gun and the first structure, while keeping the distance between the first and second accelerating structure the same. This aims to make as few changes to SwissFEL as

TABLE II. Summary of the beam dynamics performance of the current SwissFEL injector compared to the proposed injector upgrade.

Parameter	S-band SW gun [12,14]	TW rf photogun
Cathode gradient (MV/m)	100	200
Bunch charge (pC)	200	200
Extraction field strength (MV/m)	75.3	173.8
Transverse laser profile	Uniform	Uniform
Longitudinal laser profile	Uniform	Uniform
Laser beam radius (μm)	342	322
Thermal emittance (mm mrad/mm)	0.55	0.55
Laser pulse width (FWHM) (ps)	9.9	2.83
Laser pulse energy (nJ)	200	200
Energy (after gun) (MeV)	7.1	18.3
Energy (end of injector) (MeV)	130	130
Correlated energy spread (%)	0.22	0.16
Bunch length (μm)	931	326
Projected emittance (mm mrad)	0.221	0.185
Sliced emittance (mm mrad)	0.208	0.148
Peak current (A)	19.74	55.5
Central 5D brightness (TA/m^2)	905	5155

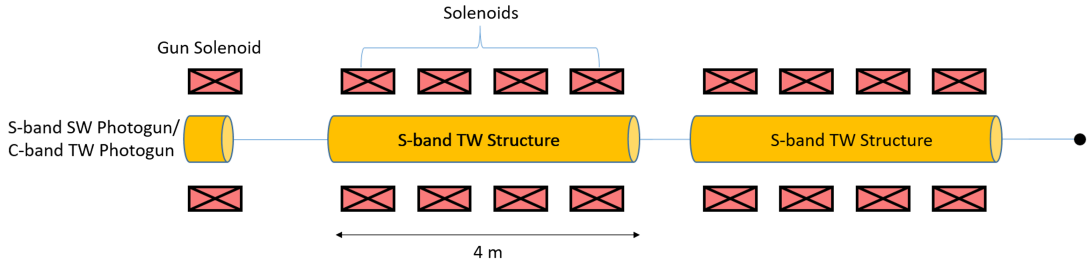

FIG. 14. Beamline setup for the simulations.

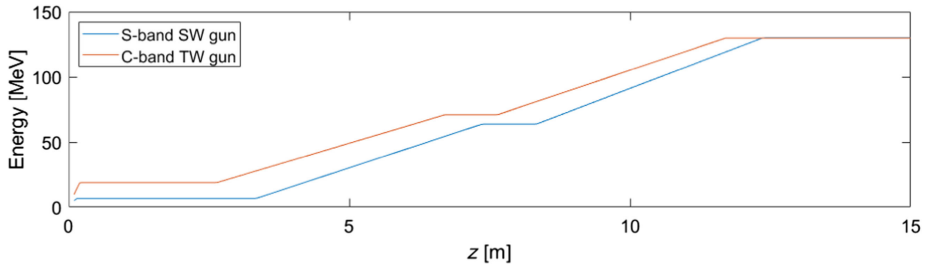

(a) Mean energy.

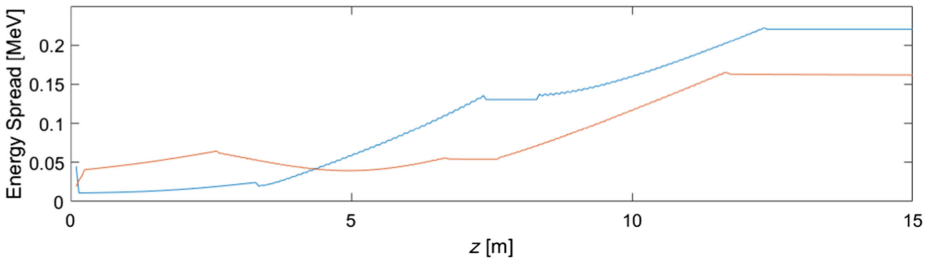

(b) Energy spread.

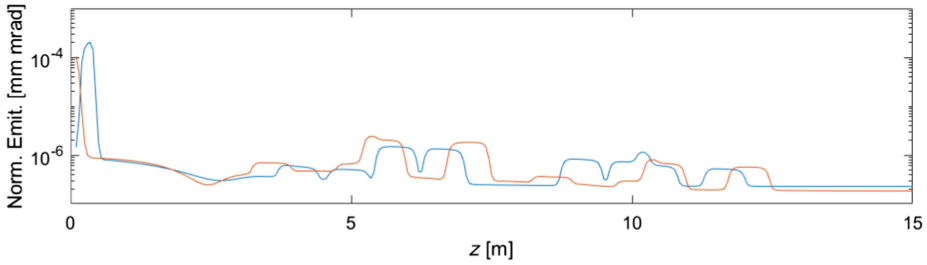

(c) Transverse emittance.

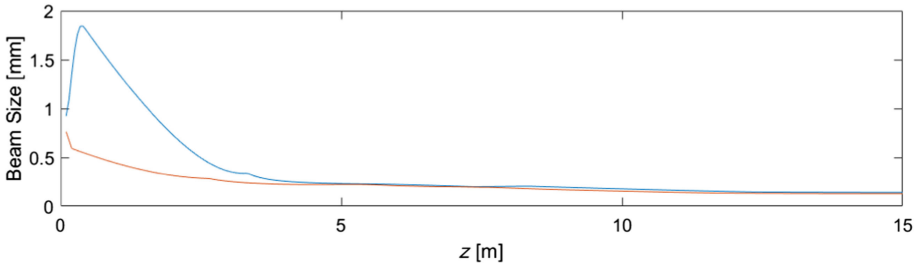

(d) Beam size.

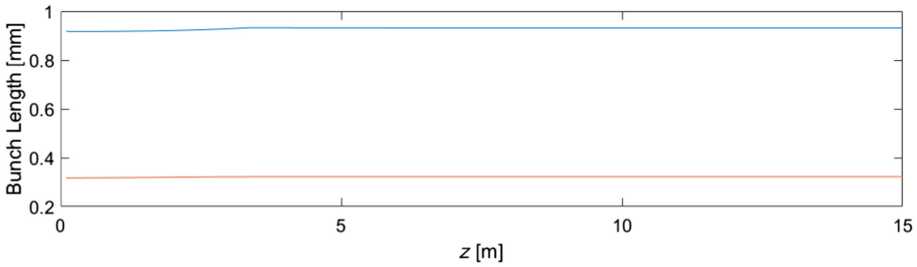

(e) Bunch length.

FIG. 15. The projected beam parameters for the current SwissFEL injector as well as the TW rf photogun for a cathode gradient of 200 MV/m.

possible while still increasing the performance making it a feasible and cost-effective upgrade to SwissFEL.

In order to find the operational points for the injector, a multivariable genetic optimization was employed. An in-depth description of this optimizer can be found in the GPT manual [28]. The optimizations were performed for a bunch with 5000 macroparticles. The goals of the optimizations were to have a projected emittance less than 0.2 mm mrad, a pulse length less than 1.2 ps and a total energy spread less than 0.1% at the end of the second structure. The measurement point for the optimization is illustrated as a spot in Fig. 14, 15 m downstream of the cathode.

The normalized emittance and bunch length relate to the sliced emittance and the peak current, and, therefore, relate to the 5D brightness [see Eq. (4)]. The beam parameters at the cathode are described in Table II. Both the S-band SW photogun and TW rf photogun cases were performed with a 200-pC bunch charge with a uniform transverse and longitudinal laser distribution. It should be noted that the uniform charge distribution is an idealized case and in practice, it is complicated to achieve particularly at short laser pulse lengths. Each situation was also assigned the same intrinsic emittance of 0.55 mm mrad/mm [29]. After the optimized value was found, the simulations were performed with 200,000 macroparticles to ensure that the solutions had converged to the correct values. Given the significant increase in the extraction electric field strength for the TW rf photogun, the electron bunch length, which was able to be maintained on the cathode, was 3.5 times shorter. It was found that the highest beam brightness came from a short bunch length on the cathode rather than a smaller laser spot size. Figure 15 illustrates the projected beam parameters along the beamline. A noticeable difference between the two situations is that the transverse and longitudinal bunch size along the beam line is significantly smaller for the TW rf photogun. This is a result of the much higher accelerating gradient and, consequently, the beam becoming more rigid when compared to the SW photogun case. The total energy spread, which is overwhelmingly

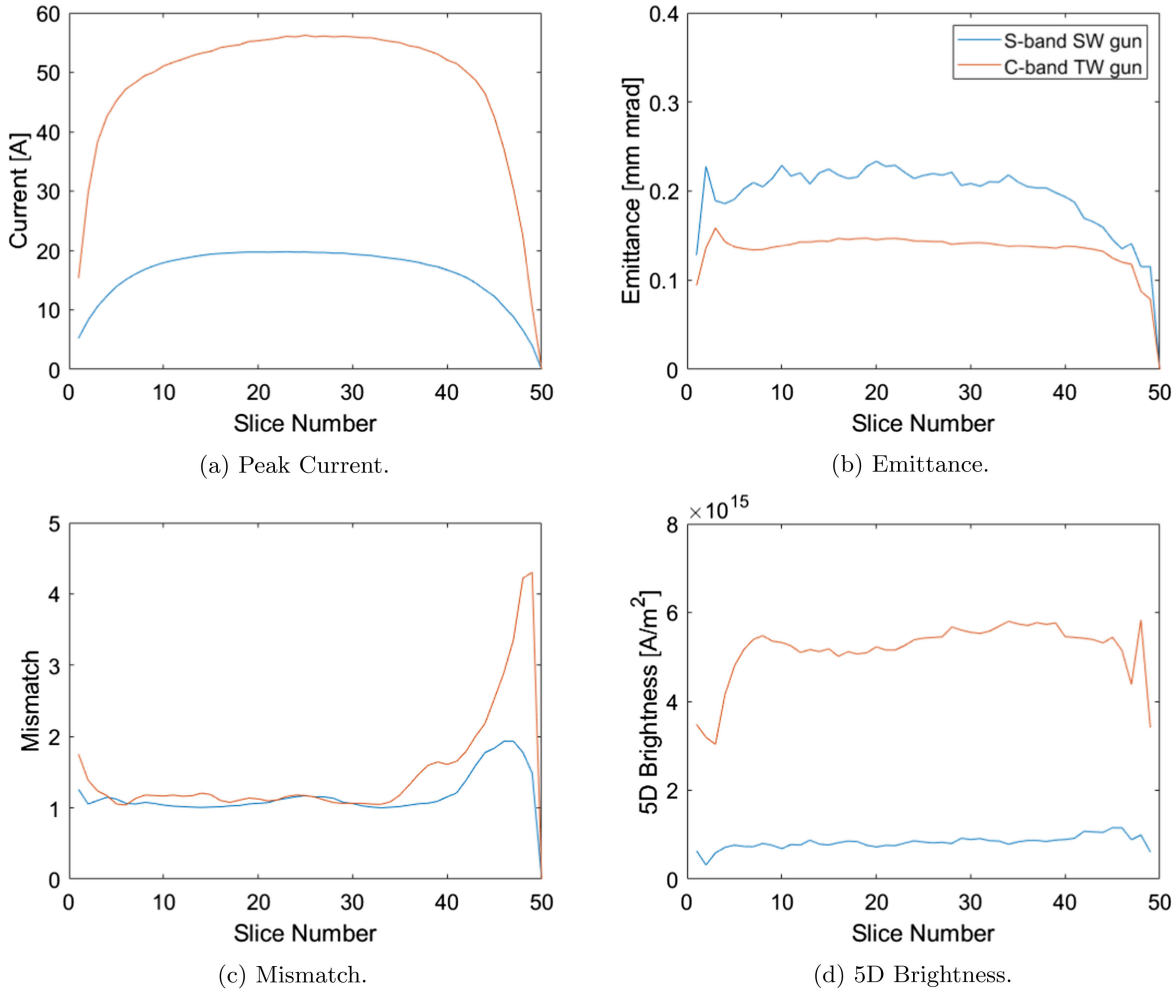

(a) Peak Current.

(b) Emittance.

(c) Mismatch.

(d) 5D Brightness.

FIG. 16. Sliced parameters at the end of the second S-band structure for the current SwissFEL injector as well as the C-band TW rf photogun for an operational gradient of 200 MV/m.

correlated energy spread, is slightly lower in the TW rf photogun case which operates with the first structure slightly off-crest and therefore is able to reduce the energy spread induced by the TW rf photogun. The normalized emittances can be seen to have very similar behavior with a modest 25% reduction for the TW rf photogun at the end of the injector. The local increases in the emittance along the injector result from the solenoids introducing an angular momentum onto the beam. Finally, what is observed is that the bunch length is primarily determined by the laser pulse length and any further changes resulting from the rf are small.

For further information on the bunch's performance in an FEL, Fig. 16 illustrates the sliced beam parameters. It is found that the peak current in the bunch increases from 19.74 to 55.5 A due to the reduced bunch length. The higher gradient also allows a slightly better emittance preservation which is 25% lower for the TW rf photogun compared to the current SwissFEL gun. These two factors combine to result in a 5D brightness of 5155 $\mathrm{TA/m^2}$ which is greater than a fivefold increase when compared to the current SwissFEL S-band SW photogun. We defined the mismatch parameter as

$$\zeta = \frac{1}{2}(\beta_0\gamma - \alpha_0\alpha + \gamma_0\beta) \geq 1, \tag{11}$$

where α, β, and γ are the sliced Twiss parameters while α_0, β_0, and γ_0 are the projected Twiss parameters. It is the goal to have this mismatch parameter as close to 1 as possible, where 1 represents a perfect matching between the transverse phase-space ellipses over the length of the bunch. The simulations results indicate that the matching between the slices is suitable for downstream lasing.

Here we have illustrated the 200 MV/m case to illustrate that the new design achieved similar results to the past design. However, in [14], it was illustrated that using a more conservative gradient of 135 MV/m already doubled the five-dimensional brightness when compared to the SwissFEL S-band gun.

VIII. MODELING OF DARK CURRENT PRODUCTION

Field emission from the cathode, and other high field regions, may limit the peak field that can be used for operation. When captured within the rf fields of an rf photogun or accelerating cavity, these field emitted electrons form a "dark current." Such dark current can degrade the beam quality extracted from the cathode, increase local radiation and, in extreme circumstances, cause beam loading within the rf cavity [30,31]. Consequently, understanding the production of this dark current within the photogun is important to understanding the high gradient limitations caused by this phenomenon. Unfortunately, to know the exact amount of dark current produced still requires experimental measurements due to the high variability of the field emission levels with respect to the level of surface conditioning [31]. Here, we aim to approximate the level of dark current produced by the TW rf photogun based on some assumptions of the surface properties and using past measurements of the SwissFEL gun [32]. The energy spectrum and transport can be modeled accurately through detailed particle tracking simulations.

In order to model the dark current produced by the TW rf photogun, we follow the approach described in [30]. To begin, the rf model (Fig. 4) was first imported into the frequency domain solver of CST MICROWAVE STUDIO. A virtual cylinder with extremely fine meshing was place around the beam axis with a radius equal to the regular cell iris radius, this was vital for the accurate generation of the field emission at the area of largest surface electric field, the cathode, as well as for the particle tracking through the photogun. The electromagnetic fieldmaps were solved in this frequency domain solver and coupled into the Particle-In-Cell (PIC) solver. The imported fieldmaps were split into two sections: the fieldmap around the cathode, where the field emission source is located, and the fieldmap in the rest of the photogun. The fieldmap around the emitter was set to step size of 20 μm while the fieldmap in the rest of the structure the step size was set to 100 μm.

In CST's PIC solver, the emission surface is set to be the cathode region and its emission properties follow the current density of the Fowler-Nordheim equation [33]. This Fowler-Nordheim equation describes the field emission process from a surface with high surface electric fields. The current density produced can be written as follows:

$$J = aE_L^2 \exp(-b/E_L), \tag{12}$$

where a and b are constants defined by the material properties, and E_L is the local electric field. The local electric field is a microscopic property of the material. We make the assumption that the microscopic field enhancement is the same across the whole surface, given no information is known on this scale and it is known that these microscopic properties vary significantly during rf conditioning [31,34]. To take into account these microscopic field effects, we set

$$E_L = \beta E_s, \tag{13}$$

where β is the field enhancement factor and E_s is the macroscopic surface electric field that has been calculated through the electromagnetic simulations [30]. The value of β is taken to be 70. This value comes from measurements on the SwissFEL rf photogun [32]. As the exact position of the field emission is not known, and in fact can change over time as mentioned above, the field emission source is distributed uniformly across the areas with the greatest

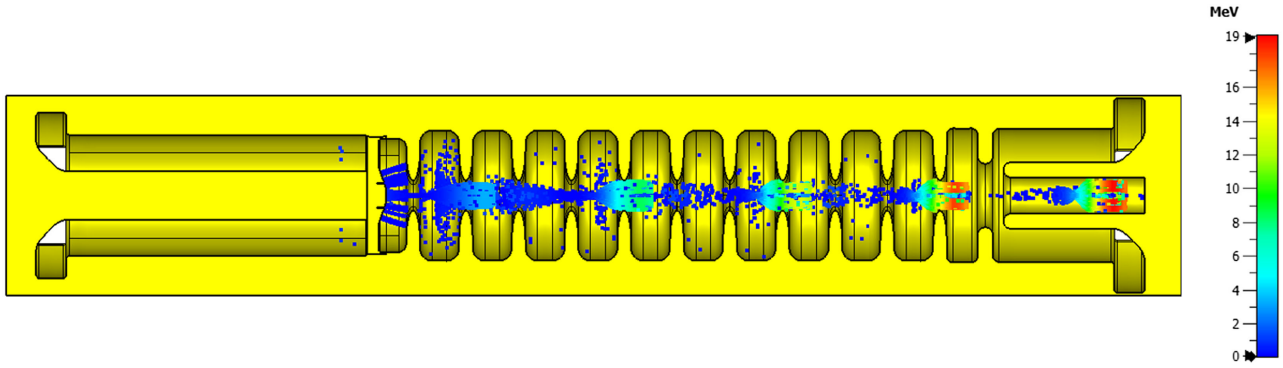

FIG. 17. The PIC model of the dark current production in the TW rf photogun.

surface electric field. In the case of the TW rf photogun, this is the entire cathode plug. The total area of field emission is set to equal the measured emission area from the SwissFEL gun which was 0.01 μm^2 with an additional scaling to account for the overall geometry difference between the two cases. Finally, the emission time-step size was refined also until the total emission no longer changed while reducing the time step.

Running the PIC solver for 10 ns allowed the PIC simulation to reach a steady-state solution. It should be noted that the simulations are for the rf fields in their steady-state solution and do not include the transient situation during the filling of the structure. For this reason, all results below will be for the situation where the structure is completely filled with rf. Figure 17 displays the PIC solver after 10 ns. It is observed that the field emitted electrons from the cathode are bunched with a separation of three cells. This is expected due to the 120-degrees phase advance regular cell design. Two important properties to investigate with the dark current simulations were the energy spectrum and bunch charges reaching the end of the structure. Figure 18(a) illustrates the energy spectrum of a single dark current bunch that reaches the end of the TW rf photogun. It is found that the dark current peaks at an energy of 18.2 MeV, which is the same as the electron bunch intended for acceleration. The level of dark current emitted from the photogun for a peak field of 200 MV/m on the cathode is expected to be high. Taking the surface properties of the SwissFEL photogun cathode, one calculates that the TW rf photogun will produce bunches of 547 and 735 fC per rf period at the end of the gun without and with the main solenoid on, respectively. This equates to a capture efficiency of 29% and 41%, respectively [Fig. 18(b)]. In the previous sections, the option of using Cs_2Te cathodes was discussed. Such cathodes are desirable for the generation of electron bunches due to their low work functions and high quantum efficiencies. However, with this reduced work function, one would expect it to impact upon the amount of dark current produced. Repeating the dark current simulations above while introducing a Cs_2Te layer on the cathode's flat region, and assuming a work function of 3.3 eV for this region, it is found that the field emission increases by approximately a factor of 15. Consequently, one expects up to 11 pC of dark current per rf period. This level of dark current may impede upon operation. However, it is yet to be seen the extent of its impact and this will be subject to investigation during the upcoming high power tests. Recent results from [11] suggest that it may be possible to significantly reduce

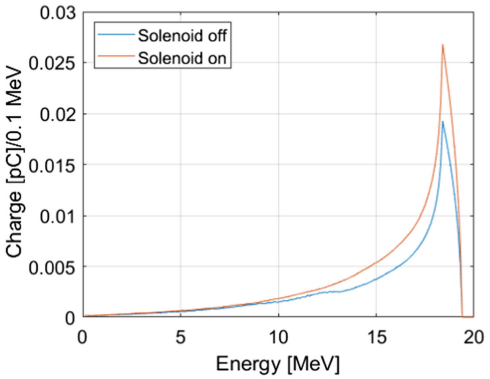

(a) Energy spectrum.

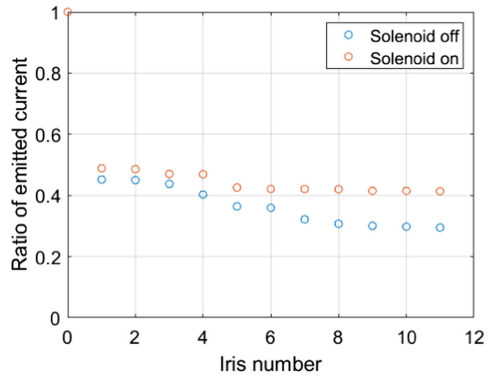

(b) Capture ratio.

FIG. 18. Properties of the dark current in the TW rf photogun.

the amount of dark current produced through increasing the surface electric field well above the operational point and then reducing the electric field for nominal operation.

IX. FURTHER DISCUSSION

In this paper, we have comprehensively presented the electromagnetic and mechanical design of the TW rf photogun and aimed to predict its ultimate performance. However, there are still some open questions which will be addressed in future work. The first of these is the mode excitation of adjacent modes due to the very short rf pulse lengths. This can be somewhat overcome by slowly ramping the rf before the flattop to reduce the bandwidth of the rf pulse. However, this would require an increase in the power dissipation reducing the possibilities of high rf pulse repetition rate operation. What makes such a study particularly complex is the broadband nature of the TW rf photogun in comparison to a SW gun which has clearly defined separate modes. Consequently, one must not just consider adjacent modes but a band of frequencies. Furthermore, such modes, along with others outside the bandwidth of the driving amplifier, may also induced by wakefields. It will be important to perform a wakefield study of the TW RF photogun to understand what limitations wakefields may play on the beam dynamics performance. Adding to the complexity of the wakefield simulations is that the first few cells where the beam is subrelativistic. The following sections are short discussions of some open questions yet to be fully explored in the TW rf photogun and will be the subject of further investigations in future work.

A. Factors contributing to sliced energy spread

A newly emerging topic for high brightness injectors, which we has yet to be addressed in this paper, is the effect of intrabeam scattering (IBS). Recently, measurements have suggested that IBS may play a key role in the sliced energy spread of the beam produced by an injector, ultimately limiting the achievable compression and performance of an FEL [35–38]. In [39], the limitations of using 5D brightness as a metric for electron source performance were discussed. It should be noted by the reader that due to the greater charge densities used in this TW rf photogun, one does expect IBS to play a more dominant role in its operation. Understanding exactly how much such effects limit the potential improvement of beam brightness is a complicated question that must take into account these effects of IBS, as well as microbunching instabilities during the bunch compression and also the reduced compression ratio required in the bunch compressor stages of the FEL when operating with shorter bunch lengths. Future investigations of the use of this TW rf photogun at SwissFEL will look at how IBS will limit its ultimate performance.

B. Sub filling-time rf pulses for the TW rf photogun

Another interesting concept for TW guns is their ability to operate with rf pulse lengths shorter than the filling time of the TW rf photogun while maintaining a nominal peak cathode field. Given the nature of traveling-wave devices, the rf field amplitude builds as the rf propagates through the structure rather than filling all cells simultaneously, as is the case for a standing-wave device. The consequences of this is that the first cell, which in the case of the traveling-wave gun contains the cathode, reach its peak electric field before the cells downstream. This peak cathode field is what is required to generate high brightness bunches and, therefore, these bunches can be generated before the rf fields finish their propagation through the structure. With this concept, it will be important to understand how the rf in the downstream cells affects the beam quality given they are still in their transient phase and the TW rf photogun's wide bandwidth. Taking Eq. (7), we see that the potential benefits from this are to operate at even greater cathode electric fields for a given breakdown rate. One could also envisage performing more intricate amplitude modulation. The potential applications of this are expected to be wide reaching. An example is that the beam energy could be changed without reducing the electric field on the cathode.

C. Heating due to the photocathode laser

One other consideration in the heating of the rf photogun is the photocathode laser. Such systems can provide significant peak power and understanding this power dissipation is important, in particular to prevent damage to the cathode. The laser parameters are described in Table II. To begin, we start with the average power dissipated by the laser. For the current SwissFEL photogun, the laser pulse energy is approximately 200 nJ for a 200-pC bunch charge and therefore we expect a similar laser pulse energy for the TW rf photogun [40]. When converting this to an average power for 100-Hz or 1-kHz operation, we find a value of 20 and 200 μW, respectively. This is several orders of magnitude below the power dissipation from the input rf. Therefore, we can neglect the laser power in steady-state temperature calculations, particularly because a significant portion of this energy is reflected from the surface and does not dissipate on the cathode.

For the pulsed heating due to the large peak power of the laser, we can make estimations of the temperature increase based on a one-dimensional semi-infinite body, similar to that used in rf pulsed surface heating (Sec. III E). The model to calculate the temperature increase on the cathode surface due to an incoming square laser pulse is given as

$$\Delta T = \frac{(1-\eta-R)F}{\sqrt{2\kappa\rho c_v \tau_l}}, \tag{14}$$

where η is the quantum efficiency, R is the reflectivity, F is the fluence, κ is thermal conductivity, ρ is the density, c_v is

the specific heat, and τ_l is the laser pulse length [41,42]. One may notice that this equation is similar to Eq. (10), which described the rf pulsed heating. For a Cs_2Te cathode, we find that it has a 40 nm layer of Cs_2Te with a copper substrate [43]. The first open question is, how much power is dissipated in the Cs_2Te and how much in the bulk Cu substrate. For completeness, one can calculate the two extreme scenarios which are as follows: the case that all the power is dissipated in the Cs_2Te layer; and the case that all the power dissipated in the Cu substrate. Taking Eq. (14) and inputting typical thermodynamic values for bulk copper, it is found that the laser pulsed heating is 6.75 K if one assumes no reflection or power loss to photoemission. For the case that all of the power dissipated into the 40-nm Cs_2Te layer, we must identify key thermodynamic properties of the material. Such properties are not widely reported in literature. Two separate studies have reported that the specific heat and thermal conductivity of Cs_2Te are 198.75 $J\,K^{-1}\,kg^{-1}$ [44] and 0.17 $W\,m^{-1}\,K^{-1}$ [45], respectively. With these values, we find that the expected temperature rise is 683 K, assuming no reflection or power losses to photoemission. The nonzero reflectivity and quantum efficiency means that this value is an overestimation. It is yet to be seen whether this causes an issue for the Cs_2Te and it may be necessary in the future to move to a new operational point for the quantum efficiency of the Cs_2Te, when compared to that used in SwissFEL. SwissFEL currently operates with a lower quantum efficiency, than that possible with Cs_2Te, in order to improve the cathode lifetime [46]. Moving to a higher quantum efficiency will reduce the required laser pulse energy and therefore laser pulsed heating, at the expense of cathode lifetime. Further studies into the use of semiconductor cathodes for the TW rf photogun will come with the realization of the device.

X. CONCLUSIONS

With the aim of producing a higher brightness electron source, a project to design, fabricate, and test the first TW rf photogun is underway at the Paul Scherrer Institute. The rf design of the TW rf photogun is based on a past design although with significant modification to the input and output couplers to ease fabrication and increase the robustness of the design. In addition to this, the mechanical design adds a load-lock capability for the exchange and use of semiconductor cathodes. Thermal simulation illustrate that this new design has the ability to operate at rf pulse repetition rates up to 1 kHz, which is highly desirable for the next generation of rf photoguns and FELs. Vacuum simulations of the complex geometry have illustrated that the vacuum level within the structure are suitable for high gradient operation although maybe a little high for sensitive semiconductor cathodes. Ultimately, when combined with a novel main solenoid, which has the bucking coil integrated into it, the TW rf photogun is able to produce a 5D brightness over 5 times greater than the current state-of-the-art S-band SW rf photoguns.

ACKNOWLEDGMENTS

The authors would like to thank Simona Bettoni for her discussions and advice on the beam dynamics. Additionally, the authors would like to thank the Fabio Cardelli, Luigi Faillace, and Gianluca Di Raddo for their monthly discussions as part of the IFAST programme. Finally, the authors would like to thanks Carlo Vicario and Romain Ganter for their discussion and advice on laser pulsed heating. This project has received funding from the European Union's Horizon 2020 Research and Innovation program under Grant Agreement No. 101004730.

[1] E. Prat *et al.*, A compact and cost-effective hard x-ray free-electron laser driven by a high-brightness and low-energy electron beam, Nat. Photonics **14**, 748 (2020).

[2] J. Rosenzweig *et al.*, Ultra-high brightness electron beams from very-high field cryogenic radiofrequency photocathode sources, Nucl. Instrum. Methods Phys. Res., Sect. A **909**, 224 (2018).

[3] M. Schaer, A. Citterio, P. Craievich, S. Reiche, L. Stingelin, and R. Zennaro, rf traveling-wave electron gun for photoinjectors, Phys. Rev. Accel. Beams **19**, 072001 (2016).

[4] A. Chao, K. Mess, M. Tigner, and F. Zimmermann, *Handbook of Accelerator Physics and Engineering* (World Scientific, Singapore, 2012).

[5] E. L. Saldin, E. V. Schneidmiller, and M. V. Yurkov, *The Physics of Free Electron Lasers* (Springer, 2000), ISBN 9783642085550.

[6] J. Rosenzweig *et al.*, Next generation high brightness electron beams from ultrahigh field cryogenic rf photocathode sources, Phys. Rev. Accel. Beams **22**, 023403 (2019).

[7] J. Rosenzweig, N. Majernik, R. Robles, G. Andonian, O. Camacho, A. Fukasawa, A. Kogar, G. Lawler, J. Miao, P. Musumeci, B. Naranjo, Y. Sakai, R. Candler, B. Pound, C. Pellegrini, C. Emma, A. Halavanau, J. Hastings, Z. Li, M. Nasr, S. Tantawi, P. Anisimov, B. Carlsten, F. Krawczyk, E. Simakov, L. Faillace, M. Ferrario, B. Spataro, S. Karkare, J. Maxson, Y. Ma, J. Wurtele, A. Murokh, A. Zholents, A. Cianchi, D. Cocco, and S. Geer, An ultra-compact x-ray free-electron laser, New J. Phys. **22**, 093067 (2020).

[8] A. Grudiev, S. Calatroni, and W. Wuensch, New local field quantity describing the high gradient limit of accelerating structures, Phys. Rev. ST Accel. Beams **12**, 102001 (2009).

[9] P. Wilson and J. Griffin, High energy electron linacs; application to storage ring RF systems and linear colliders, AIP Conf. Proc. **87**, 450 (1982).

[10] T. Wangler, *RF Linear Accelerators* (Wiley, New York, 2008), ISBN 9783527406807.

[11] W. Tan, S. Antipov, D. Doran, G. Ha, C. Jing, E. Knight, S. Kuzikov, W. Liu, X. Lu, P. Piot, J. Power, J. Shao, C. Whiteford, and E. Wisniewski, Demonstration of

sub-GV/m accelerating field in a photoemission electron gun powered by nanosecond X-band radio-frequency pulses, Phys. Rev. Accel. Beams **25**, 083402 (2022).

[12] J.-Y. Raguin, M. Bopp, A. Citterio, and A. Scherer, The SwissFEL RF gun: RF design and thermal analysis, in *Proceedings of LINAC2012, Tel-Aviv, Israel* (JACoW, Geneva, Switzerland, 2012), TUPLB01.

[13] D. Alesini, F. Cardelli, G. Castorina, M. Croia, G. Di Raddo, L. Faillace, M. Ferrario, L. Ficcadenti, A. Giribono, A. Gizzi, S. Lauciani, A. Liedl, G. Pedrocchi, L. Pellegrino, L. Piersanti, C. Vaccarezza, and A. Vannozzi, The new C band gun for the next generation RF photoinjectors, in *Proceedings of 13th International Particle Acclerator Conference, IPAC2022, Bangkok, Thailand* (JACoW, Geneva, Switzerland, 2022), pp. 679–682.

[14] M. Schaer, RF traveling-wave electron gun for high brightness photoinjectors, Ph.D. thesis, ETH Zurich, 2016.

[15] 3DS CST Microwave Studio, https://www.3ds.com/.

[16] H. Zha, J. Shi, H. Chen, A. Grudiev, W. Wuensch, C. Tang, and W. Huang, Choke-mode damped structure design for the Compact Linear Collider main linac, Phys. Rev. ST Accel. Beams **15**, 122003 (2012).

[17] R. Ganter *et al.*, SwissFEL cathode load-lock system, in *Proceedings of the 35th International Free-Electron Laser Conference, FEL2013, New York, NY* (JACoW, Geneva, Switzerland, 2013), TUPSO21.

[18] A. Gaponov and M. Miller, On the potential well for charged particles in a high frequency electromagnetic field, Sov. Phys. JETP **34**, 168 (1958), http://jetp.ras.ru/cgi-bin/dn/e_007_01_0168.pdf.

[19] D. Pritzkau, RF pulsed heating, Ph.D. thesis, Stanford University, 2001.

[20] ANSYS HFSS, https://www.ansys.com/.

[21] ANSYS Fluent, https://www.ansys.com/.

[22] K. Papke, C. Rossi, and G. Burt, Coupled rf-thermo-structural analysis of CLIC traveling wave accelerating structures, CERN Report No. CLIC–Note–1158, 2020.

[23] R. Kersevan and M. Ady, Recent developments of Monte-Carlo codes Molflow+ and Synrad+, in *Proceedings of 10th Particle Accelerator Conference, IPAC2019, Melbourne, Australia* (JACoW, Geneva, Switzerland, 2019).

[24] P. Chiggiato, Outgassing properties of vacuum materials for particle accelerators, arXiv:2006.07124.

[25] E. Colby, Design, construction, and testing of a radio-frequency electron photoinjector for the next generation linear collider, Ph.D. thesis, Office of Scientific, 1997.

[26] L. Conradie, Magnet design, in *Proceedings of Joint ICTP/IAEA Workshop on Accelerator Technologies, Basic Instruments and Analytical Techniques* (2019), https://indico.ictp.it/event/8728/session/6/contribution/22/material/slides/0.pdf.

[27] S. L. Sobolev, *Partial Differential Equations of Mathematical Physics* (Elsevier, New York, 1964), ISBN 9780080104249.

[28] Pulsar Physics General Particle Tracer (GPT) (2021,1,25), www.pulsar.nl/gpt.

[29] R. Marsh, G. Anderson, S. Anderson, D. Gibson, C. Barty, and Y. Hwang, Performance of a second generation X-band rf photoinjector, Phys. Rev. Accel. Beams **21**, 073401 (2018).

[30] T. Lucas, T. Argyopolous, M. Boland, N. Catalan-Lasheras, R. Rassool, C. Serpico, M. Volpi, and W. Wuensch, Dependency of the capture of field emitted electron on the phase velocity of a high-frequency accelerating structure, Nucl. Instrum. Methods Phys. Res., Sect. A **914**, 46 (2019).

[31] T. Lucas, High field phenomenology in linear accelerators for the compact linear collider, School of Physics, University of Melbourne, 2018.

[32] S. Bettoni, P. Craievich, M. Pedrozzi, M. Schaer, and L. Stingelin, Low energy dark current collimation system in single-pass linacs, Phys. Rev. Accel. Beams **21**, 023401 (2018).

[33] R. Fowler and L. Nordheim, Electron emission in intense electric fields, Proc. R. Soc. A **119**, 173 (1928).

[34] D. Banon-Caballero, M. Boronat, N. Catalán-Lasheras, A. Faus-Golfe, B. Gimeno, T. Lucas, W. Millar, J. Paszkiewicz, S. Pitman, V. Sánchez Sebastián, A. Vnuchenko, M. Volpi, M. Widorski, W. Wuensch, and V. Del Pozo Romano, Dark current analysis at CERN's X-band Facility, in *Proceedings of 10th Particle Accelerator Conference, IPAC2019, Melbourne, Australia* (JACoW, Geneva, Switzerland, 2019), pp. 2944–2947.

[35] E. Prat, P. Craievich, P. Dijkstal, S. Di Mitri, E. Ferrari, T. Lucas, A. Malyzhenkov, G. Perosa, S. Reiche, and T. Schietinger, Energy spread blowup by intrabeam scattering and microbunching at the SwissFEL injector, Phys. Rev. Accel. Beams **25**, 104401 (2022).

[36] H. Qian, M. Krasilnikov, A. Lueangaramwong, X. Li, O. Lishilin, Z. Aboulbanine, G. Adhikari, N. Aftab, P. Boonpornprasert, G. Georgiev, J. Good, M. Gross, C. Koschitzki, R. Niemczyk, A. Oppelt, G. Shu, F. Stephan, G. Vashchenko, and T. Weilbach, Slice energy spread measurement in the low energy photoinjector, Phys. Rev. Accel. Beams **25**, 083401 (2022).

[37] S. Tomin, I. Zagorodnov, W. Decking, N. Golubeva, and M. Scholz, Accurate measurement of uncorrelated energy spread in electron beam, Phys. Rev. Accel. Beams **24**, 064201 (2021).

[38] E. Prat, P. Dijkstal, E. Ferrari, A. Malyzhenkov, and S. Reiche, High-resolution dispersion-based measurement of the electron beam energy spread, Phys. Rev. Accel. Beams **23**, 090701 (2020).

[39] T. Lucas, A discussion of key concepts for the next generation of high brightness injectors, in *Proceedings of 31st Linear Accelerator Conference, LINAC2022, Liverpool, UK* (JACoW, Geneva, Switzerland, 2022).

[40] C. Vicario, R. Ganter, F. Le Pimpec, C. Hauri, S. Hunziker, C. Ruchert, T. Schietinger, and A. Trisorio, Photocathode drive laser for SwissFEL, in *Proceedings of FEL2010, Malmö, Sweden* (JACoW, Geneva, Switzerland, 2010).

[41] X. E. Lin, Laser pulse heating, in *Proceedings of the 18th Particle Accelerator Conference, New York, 1999* (IEEE, New York, 1999).

[42] E. Sabia, A. Dipace, C. R. Portici, and G. Dattoli, Free electron laser triggered photo-cathode, in *Proceedings of 28th International Particle Accelerator Conference, FEL2006, BESSY, Berlin, Germany* (JACoW, Geneva, Switzerland, 2006).

[43] J. Bossert, R. Ganter, M. Schaer, and T. Schietinger, Cu and Cs2Te cathodes preparation and QE history at the SwissFEL Injector Test Facility, in *Proceedings of 36th International Free Electron Laser Conference (FEL2014)* (JACoW Publishing, Geneva, Switzerland, 2014).

[44] S. Zeng, L. Fang, Y. Tu, M. Zulfiqar, and G. Li, Ultralow lattice thermal conductivity of binary compounds $A_2B(A = Cs,\ Rb\ \&\ B = Se, Te)$ with higher-order anharmonicity correction, Phys. Chem. Chem. Phys. **25**, 12157 (2023).

[45] E. H. P. Cordfunke, W. Ouweltjes, J. C. Van Miltenburg, and A. Schuijff, The thermodynamic properties of di-caesium telluride, Cs_2Te, from 5 to 800 K, J. Chem. Thermodyn. **19**, 293 (1987).

[46] Personal correspondence with Carlo Vicario and Romain Ganter.